This is an open access article published under an ACS AuthorChoice License, which permits copying and redistribution of the article or any adaptations for non-commercial purposes.

ACS central science

http://pubs.acs.org/journal/acscii

Research Article

Revisiting the $Na_{2/3}Ni_{1/3}Mn_{2/3}O_2$ Cathode: Oxygen Redox Chemistry and Oxygen Release Suppression

Yi Zhang, Miaomiao Wu, Jiwei Ma, Guangfeng Wei, Yun Ling, Renyuan Zhang,* and Yunhui Huang*

Cite This: *ACS Cent. Sci.* 2020, 6, 232−240

Read Online

ACCESS | Metrics & More | Article Recommendations | Supporting Information

ABSTRACT: Sodium layered transition metal oxides have been considered as promising cathode materials for sodium ion batteries due to their large capacity and high operating voltage. However, mechanism investigations of chemical evolution and capacity failure at high voltage are inadequate. As a representative cathode, $Na_{2/3}Ni_{1/3}Mn_{2/3}O_2$, the capacity contribution at a 4.2 V plateau has long been assigned to the redox of the Ni^{3+}/Ni^{4+} couple, while at the same time it suffers large irreversible capacity loss during the initial discharging process. In this work, we prove that the capacity at the 4.2 V plateau is contributed to the irreversible $O^{2-}/O_2^{n-}/O_2$ evolution based on in situ differential electrochemical mass spectrometry and density functional theory calculation results. Besides, a phenomenon of oxygen release and subsequent surface lattice densification is observed, which is responsible for the large irreversible capacity loss during the initial cycle. Furthermore, the oxygen release is successfully suppressed by Fe substitution due to the formation of a unique Fe-(O−O) species, which effectively stabilizes the reversibility of the O^{2-}/O_2^{n-} redox at high operating voltage. Our findings provide a new understanding of the chemical evolution in layered transition metal oxides at high operating voltage. Increasing the covalency of the TM−O bond has been proven to be effective in suppressing the oxygen release and hence improving the electrochemical performance.

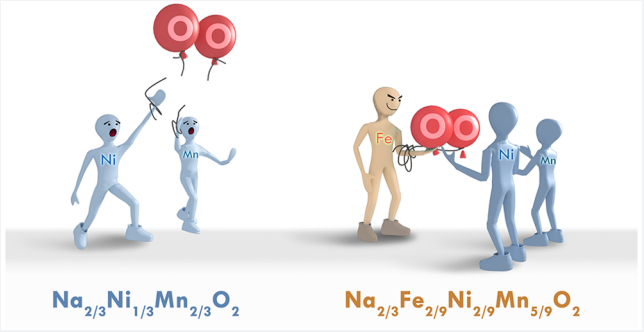

INTRODUCTION

Rechargeable sodium-ion batteries (SIB) are regarded as a highly promising alternative to commercialized lithium-ion batteries (LIB) for grid energy storage applications because of the richer natural abundance and relatively lower cost of Na resources.[1−7] Since the discovery of the Na_xCoO_2 cathode by Delmas in 1981,[8] various sodium layered transition metal oxides (Na_xTMO_2) have been investigated as a Na-ion host.[9−13] In 2001, Lu et al. first reported that P2-$Na_{2/3}Ni_{1/3}Mn_{2/3}O_2$ delivered a large capacity (about 165 mAh g^{-1}) with a high operating voltage.[14,15] After that, most of following research on $Na_{2/3}Ni_{1/3}Mn_{2/3}O_2$ claimed that the capacity in the voltage range of $2.2 \le V \le 4.1$ (~85 mAh g^{-1}) is contributed by the Ni^{2+}/Ni^{3+} redox couple, and the capacity around the 4.2 V long plateau (~80 mAh g^{-1}) is associated with the Ni^{3+}/Ni^{4+} couple.[16−21] However, this viewpoint has recently been faced with challenges.[22,23] In 2017, Ma et al. designed a TM-deficient (TM = transition metal) $Na_{0.78}Ni_{0.23}Mn_{0.69}O_2$ compound ($Na_xTM_yO_2$, $y < 1$) and proved that Ni^{2+} was oxidized to Ni^{4+} when charged to 4.1 V, while the plateau above 4.2 V was dominated by the O^{2-}/O_2^{n-} couple due to TM vacancies.[22] In 2018, Risthaus et al. observed the change of oxygen state at 4.5 V in $Na_{2/3}Ni_{1/3}Mn_{2/3}O_2$.[23] Therefore, it is necessary to determine the sodium storage mechanism and capacity contribution around the 4.2 V plateau.

Besides, the $Na_{2/3}Ni_{1/3}Mn_{2/3}O_2$ cathode suffers rapid capacity degradation during the charging/discharging process. Numerous research studies focus on the structure evolution, and it is believed that the "P2 → O2 phase transition" is the main reason because it can cause large volume variation (about 20%).[16−21,24] Strategies such as element doping[17−20,25] or inert layer coating[26,27] are commonly used to suppress the phase transition or alleviate the volume change. However, a large irreversible capacity loss still occurs during the initial cycle. Wu et al. designed a $Na_{0.67}Ni_{0.26}Zn_{0.07}Mn_{0.67}O_2$ cathode without the P2 → O2 phase transition and found 14% irreversible capacity loss at the first cycle.[25] Liu et al. modified the $Na_{2/3}Ni_{1/3}Mn_{2/3}O_2$ surface with an Al_2O_3 buffer layer and observed a 16% irreversible capacity sacrifice during the first cycle.[26] The TM-deficient $Na_{0.78}Ni_{0.23}Mn_{0.69}O_2$ compound also suffered a 23% irreversible capacity loss at the first cycle.[22] It is highly probable that the previous studies on the failure mechanism of $Na_{2/3}Ni_{1/3}Mn_{2/3}O_2$ are not comprehensive. Therefore, understanding the mechanism for this irreversible capacity loss at the

Received: November 12, 2019
Published: January 29, 2020

© 2020 American Chemical Society

https://dx.doi.org/10.1021/acscentsci.9b01166
ACS Cent. Sci. 2020, 6, 232−240

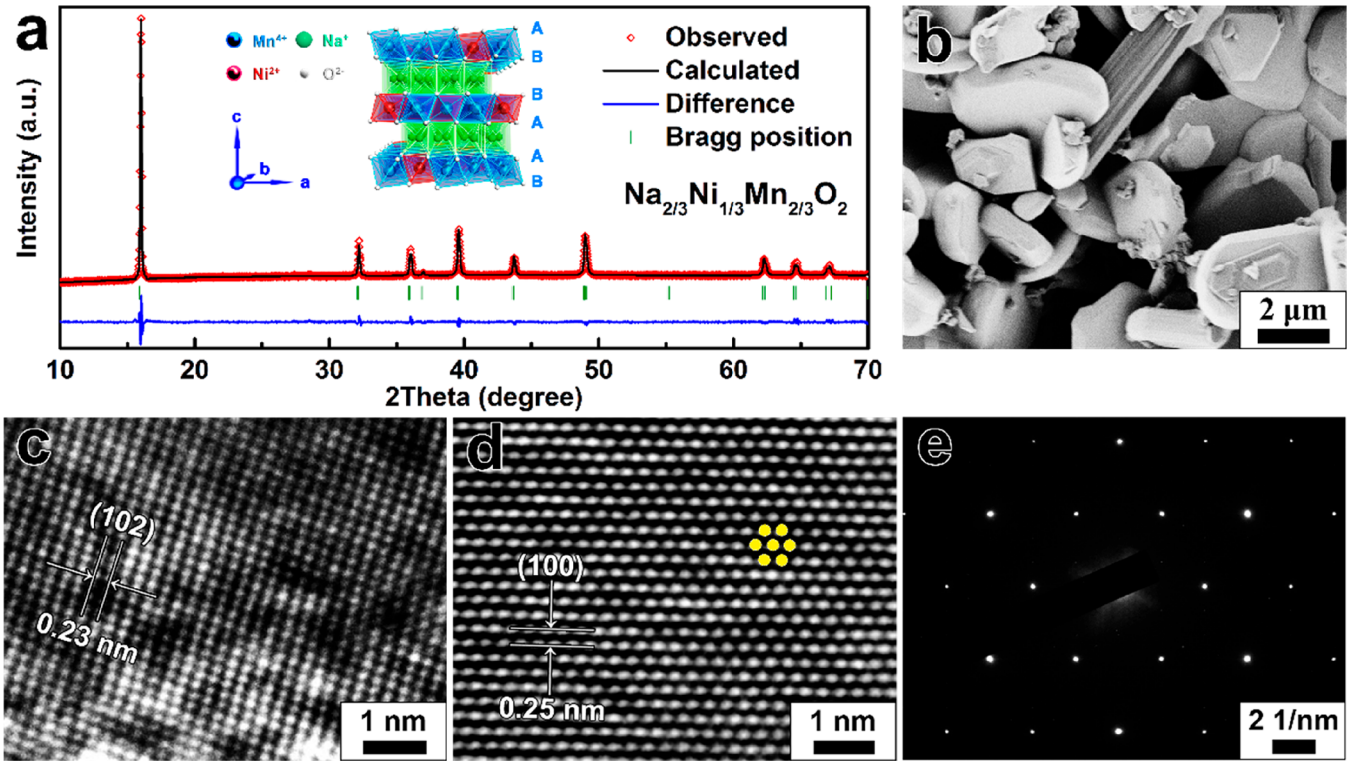

Figure 1. (a) XRD pattern and Rietveld refinement of the $Na_{2/3}Ni_{1/3}Mn_{2/3}O_2$ sample. The inset shows the P2 type structure with "ABBAAB" arrangement. (b) SEM image of $Na_{2/3}Ni_{1/3}Mn_{2/3}O_2$ particles. (c–d) 102 and 100 planes of $Na_{2/3}Ni_{1/3}Mn_{2/3}O_2$. (e) The corresponding SAED image of $Na_{2/3}Ni_{1/3}Mn_{2/3}O_2$.

initial cycle and solving the capacity degradation problem have become an urgent issue with great significance.

In this work, we present an evident understanding of the chemical evolution in $Na_{2/3}Ni_{1/3}Mn_{2/3}O_2$. We find that the capacity around the 4.2 V plateau is dominated by oxygen redox according to the X-ray photoelectron spectroscopy (XPS) analysis combined with density functional theory (DFT) calculations. Meanwhile, the oxygen release behavior of $Na_{2/3}Ni_{1/3}Mn_{2/3}O_2$ is observed via in situ differential electrochemical mass spectrometry (DEMS). At the high voltage region, the oxygen functions as the electron donor, and the irreversible $O^{2-}/O_2^{n-}/O_2$ evolution occurs due to the lack of TM-O hybridization. Significantly, we find that the loss of O_2 gas causes surface densification on $Na_{2/3}Ni_{1/3}Mn_{2/3}O_2$ particles. According to the calculated results, this dense surface is not available for Na^+ intercalation, resulting in a large irreversible capacity loss at the initial cycle. Accordingly, we propose a highly efficient method to suppress the oxygen release behavior in $Na_{2/3}Ni_{1/3}Mn_{2/3}O_2$ by Fe doping to form Fe-(O–O) species associated with reductive coupling behavior. The well-designed $Na_{2/3}Fe_{2/9}Ni_{2/9}Mn_{5/9}O_2$ SIB cathode material shows an excellent reversibility of the O^{2-}/O_2^{n-} couple at high operating voltage, which reduces the irreversible capacity loss from 25% to 4% at the initial cycle. The specific energy density is achieved as high as 500 Wh kg^{-1} with excellent cycling stability.

RESULTS AND DISCUSSION

Oxygen Redox Activity in $Na_{2/3}Ni_{1/3}Mn_{2/3}O_2$. P2-$Na_{2/3}Ni_{1/3}Mn_{2/3}O_2$ was synthesized through a simple sol–gel method followed by high-temperature treatment under O_2 atmosphere. As illustrated in Figure 1a, the crystal structure of P2-$Na_{2/3}Ni_{1/3}Mn_{2/3}O_2$ is built on the alternate arrangement of Na^+ layers and TM ions layers. All the Na ions occupy the "prismatic" sites, and the oxygen ion framework is stacked with "ABBA" mode. The X-ray diffraction (XRD) pattern of P2-$Na_{2/3}Ni_{1/3}Mn_{2/3}O_2$ is indexed to the hexagonal $P6_3/mmc$ space group. The refined crystallographic data are listed in Table S1. Figure 1b shows the SEM image of the $Na_{2/3}Ni_{1/3}Mn_{2/3}O_2$ particles with a hexagonal shape. The 102 and 100 planes are clearly observed in Figure 1c and d, respectively. The corresponding selected area electron diffraction (SAED) pattern in Figure 1e confirms that the $Na_{2/3}Ni_{1/3}Mn_{2/3}O_2$ sample has the typical single-crystal characteristics.

To investigate the chemical evolution in $Na_{2/3}Ni_{1/3}Mn_{2/3}O_2$ in detail, the XPS spectra were collected at various states (Figure 2 and Figure S1, marked with I, II, III, IV, and V). For the Mn element, the binding energy of the Mn 2p peaks almost remains unchanged during the whole charge/discharge process ($2.6 \leq V \leq 4.3$); hence, Mn^{4+} is not involved in the electrochemical reaction. For the Ni element, the Ni 2p peak at 854.4 eV shifts toward a higher binding energy (855 eV) from point I to II, indicating the occurrence of the Ni^{2+}/Ni^{3+} oxidation reaction below 4.2 V.[28−31] However, all Ni^{3+} peaks show no shift from point II to III, demonstrating that Ni still maintains a trivalent state without oxidation in this region. As the charging process continues, a small peak of 858.1 eV starts to appear at point IV (4.3 V), which could be assigned to Ni^{4+}.[29,30,32] This Ni^{4+} shoulder peak gets stronger when the voltage reaches 4.5 V (Figure S2). Therefore, the main voltage region for the Ni^{3+}/Ni^{4+} reaction is above 4.3 V, while the charge compensation process at the 4.2 V plateau shows almost no correlation to the oxidation of Ni^{3+}. To further verify this viewpoint, all Ni^{2+} ions in $Na_{2/3}Ni_{1/3}Mn_{2/3}O_2$ were replaced by Mn^{4+} for the charge/discharge test (Figure S3a,b). As illustrated in Figure S3d, the

https://dx.doi.org/10.1021/acscentsci.9b01166
ACS Cent. Sci. 2020, 6, 232−240

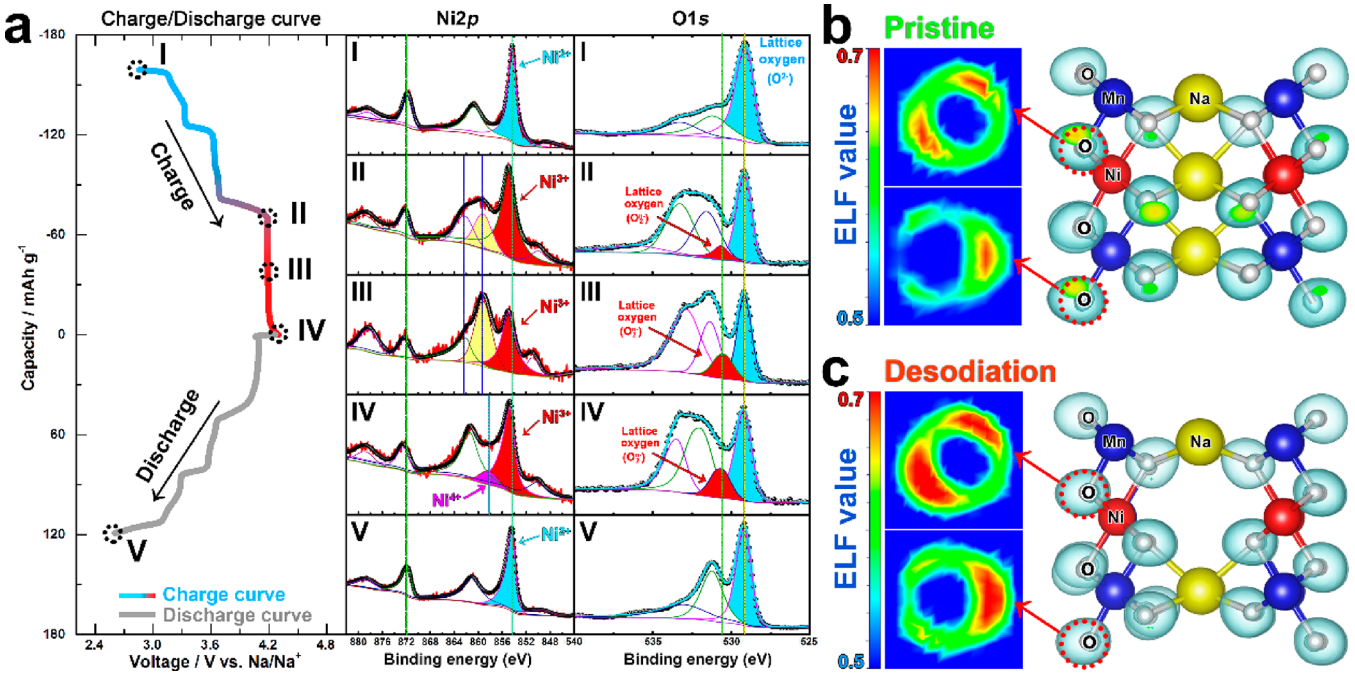

Figure 2. (a) Galvanostatic charge/discharge curves of the $Na_{2/3}Ni_{1/3}Mn_{2/3}O_2$ electrode for the first cycle at 0.1 C and the corresponding XPS spectra of Ni 2p and O 1s core at various charge states. (b−c) Representative ELF cross sections of lattice oxygen at pristine and desodiation (charged to 4.2 V) states, respectively. The oxygen lone-pair tends to locate at a position with a high ELF value.

Ni-free counterpart of the $Na_{2/3}Mn_{5/6}O_2$ compound still shows a long plateau at 4.2 V with a capacity of about 60 mAh g^{-1}. For the O element, only lattice O^{2-} anions peaks (529.5 eV) exist in a pristine state (point I). However, an extra O 1s peak emerges at 530.5 eV when charged to 4.2 V (point II), which can be attributed to the formation of the O_2^{n-} species.[33−37] From point II to IV, this O_2^{n-} peak becomes stronger gradually, indicating that the charge compensation process at the 4.2 V plateau is dominated by the O^{2-}/O_2^{n-} couple.

The participation of lattice oxygen in the charge compensation process is relevant to the oxygen lone-pair.[38−40] Here, electron localization function (ELF) was employed to characterize and visualize the oxygen lone-pair in $Na_{2/3}Ni_{1/3}Mn_{2/3}O_2$. The area with a high ELF value (red zone) signifies the position with lone-pairs, while the value of 0.5 (blue zone) corresponds to an electron gas-like pair probability.[41,42] At the pristine stage (Figure 2b), the lone-pair area in lattice oxygen is rather limited. When charged to 4.2 V (0.33 Na^+ removal), the area for lone-pair electrons becomes more extensive (Figure 2c), indicating that the lattice oxygen tends to participate in the electrochemical reaction at a high operating voltage.

Oxygen Release and Surface Densification. In situ DEMS was employed to analyze the gas release behavior of $Na_{2/3}Ni_{1/3}Mn_{2/3}O_2$ during the charge process (Figure 3a and Figure S4). When the electrode was charged from the initial state to 4.2 V, no O_2 release was detected. However, a sudden increase of O_2 gas flux was observed from 4.2 to 4.3 V, indicating the oxygen loss behavior of $Na_{2/3}Ni_{1/3}Mn_{2/3}O_2$ at high operating voltage. On the basis of the calculation results, 0.0061 mol of O_2 gas was released per mol of $Na_{2/3}Ni_{1/3}Mn_{2/3}O_2$ at 4.3 V high voltage. To understand this phenomenon, density of states (DOS) is calculated at 4.2 V (0.33 Na^+ removal) and 4.3 V (0.6 Na^+ removal) to investigate the chemical evolution of O^{2-} (Figure 3b). The O 2p band exceeds the Fermi level from 4.2 to 4.3 V, demonstrating that the charge compensation process is mainly carried out by the oxidation of lattice oxygen in this voltage region, which agrees with the XPS result of O spectra and the ELF results (Figure 2). However, there is almost no Ni or Mn 3d band overlap in the front part of the O 2p band at 4.3 V, which probably leads to the decoordination of the O_2^{n-} species and even the loss of oxygen because of the lack of TM-O hybridization (Figure 3c).[33,39,43,44] Meanwhile, the whole charge process shows a large capacity of 158 mAh g^{-1}, but only 119 mAh g^{-1} is delivered during the subsequent discharge process, implying the large irreversible capacity loss (25%) at the initial cycle (Figure 3d). We consider that this severe capacity loss is related to the irreversible evolution of $O^{2-}/O_2^{n-}/O_2$ in $Na_{2/3}Ni_{1/3}Mn_{2/3}O_2$.

O_2 release in a Li-rich compound usually causes undesired crystal reconstruction.[33−35,45−47] HRTEM was used to analyze the crystal structure evolution of $Na_{2/3}Ni_{1/3}Mn_{2/3}O_2$ during the charge/discharge process. At the pristine stage, the interlayer distance at surface is 0.56 nm (Figure 3e), corresponding to the 002 plane. However, after one cycle in the voltage range between 2.6 and 4.3 V, a new structure with a contracted interlayer distance of 0.25 nm is formed on the particle surface (Figure 3f), which still exists after 10 cycles (Figure S5a). The dense layer compound can not be detected by XRD analysis due to the trace amount (Figure S5b). Therefore, we can only propose a probable $Ni_2Mn_2O_7$ structure with an interlayer distance of 0.25 nm for this dense layer based on DFT calculations (Figure 3g). According to the calculated results, when Na^+ ions insert into the interlayer space of the $Ni_2Mn_2O_7$ compound, the ΔE (ΔE is the energy difference of the $Ni_2Mn_2O_7$ system in which a Na atom is embedded) shows a huge increase, proving that the dense layer is not suitable for Na^+ intercalation (Figure S6). Therefore, we consider that the formation of the inactive dense surface caused by oxygen release is the main reason for the large irreversible capacity loss at the initial cycle.

https://dx.doi.org/10.1021/acscentsci.9b01166
ACS Cent. Sci. 2020, 6, 232−240

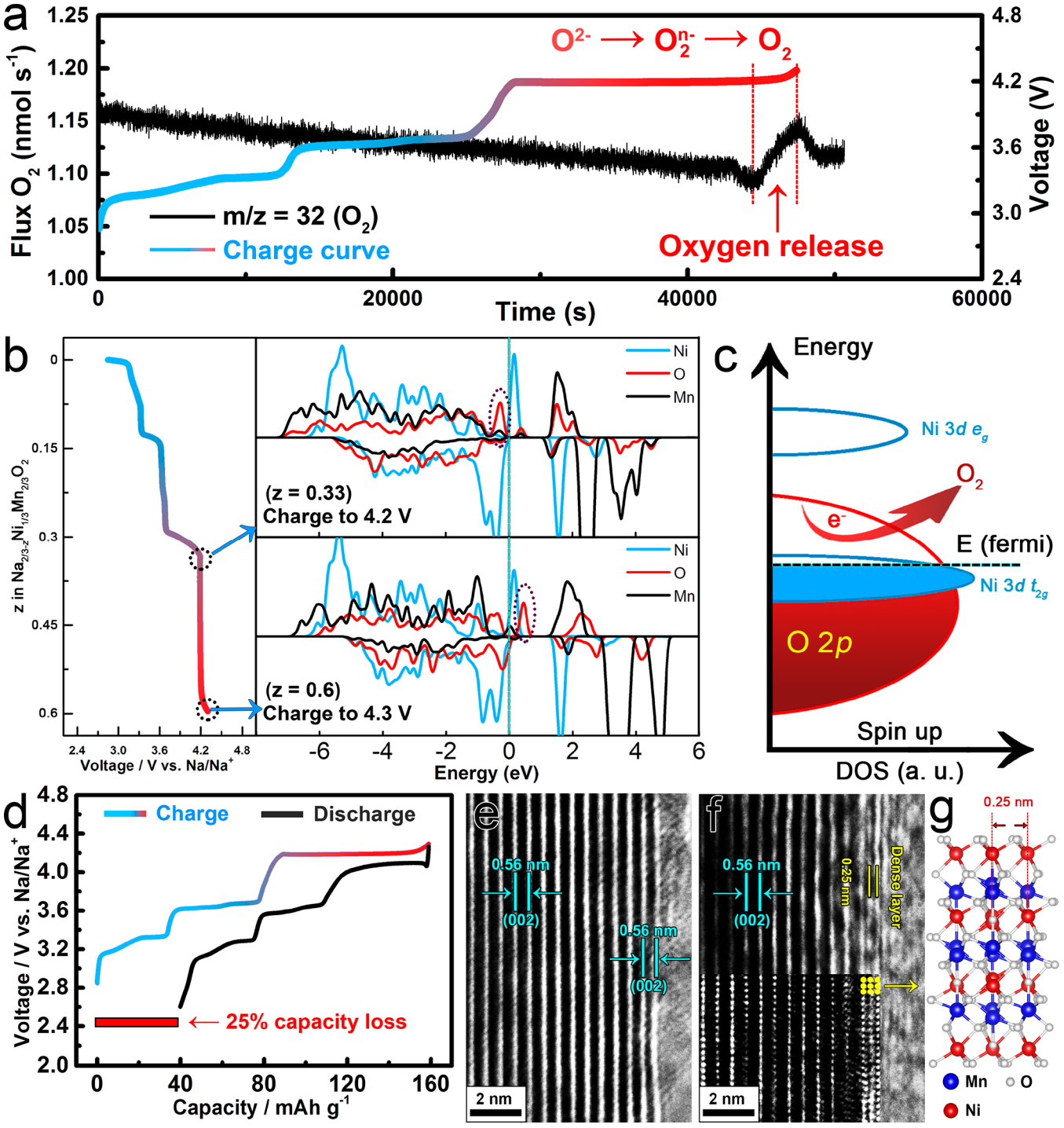

Figure 3. (a) In situ DEMS analysis of oxygen release during the first charge for the $Na_{2/3}Ni_{1/3}Mn_{2/3}O_2$ electrode. The charge current density is 10 μA mg^{-1}, and the cut off voltage is 4.3 V. (b) DOS of $Na_{2/3}Ni_{1/3}Mn_{2/3}O_2$ cathode at 4.2 V (0.33 Na removal) and 4.3 V (0.6 Na removal). The Fermi level is indicated by the dash line. (c) Schematic representation of the energy level versus DOS and the loss of oxygen. (d) Galvanostatic charge/discharge curves of $Na_{2/3}Ni_{1/3}Mn_{2/3}O_2$ electrode and the irreversible capacity loss for the first cycle at 0.1 C. (e) HRTEM image of $Na_{2/3}Ni_{1/3}Mn_{2/3}O_2$ at the pristine state. (f) HRTEM image of $Na_{2/3}Ni_{1/3}Mn_{2/3}O_2$ after one cycle. (g) The calculated structure of the dense surface.

Suppressing of Oxygen Release. Since the oxygen release behavior seriously affects the crystal structure as well as electrochemical performance of $Na_{2/3}Ni_{1/3}Mn_{2/3}O_2$, how to address this issue is of great significance. Previous research on the Li-rich $Li_2Ru_{1-y}Sn_yO_3$ cathode suggested that Ru^{5+} could form a Ru−O−O covalent bond to minimize oxygen release at a high operating voltage.[34] Considering the similar electronic configuration of Fe and Ru, we employ Fe substitution to suppress the oxygen release behavior in $Na_{2/3}Ni_{1/3}Mn_{2/3}O_2$. By replacing Ni^{2+} and Mn^{4+} with Fe^{3+}, the $Na_{2/3}Fe_{2/9}Ni_{2/9}Mn_{5/9}O_2$ cathode was synthesized under the same condition as $Na_{2/3}Ni_{1/3}Mn_{2/3}O_2$.

The XRD pattern of $Na_{2/3}Fe_{2/9}Ni_{2/9}Mn_{5/9}O_2$ reveals that the substitution of Fe^{3+} still maintains the original hexagonal structure with $P6_3/mmc$ space group (Figure 4a). The refined crystallographic data are listed in Table S1. Figure 4b shows the

https://dx.doi.org/10.1021/acscentsci.9b01166
ACS Cent. Sci. 2020, 6, 232−240

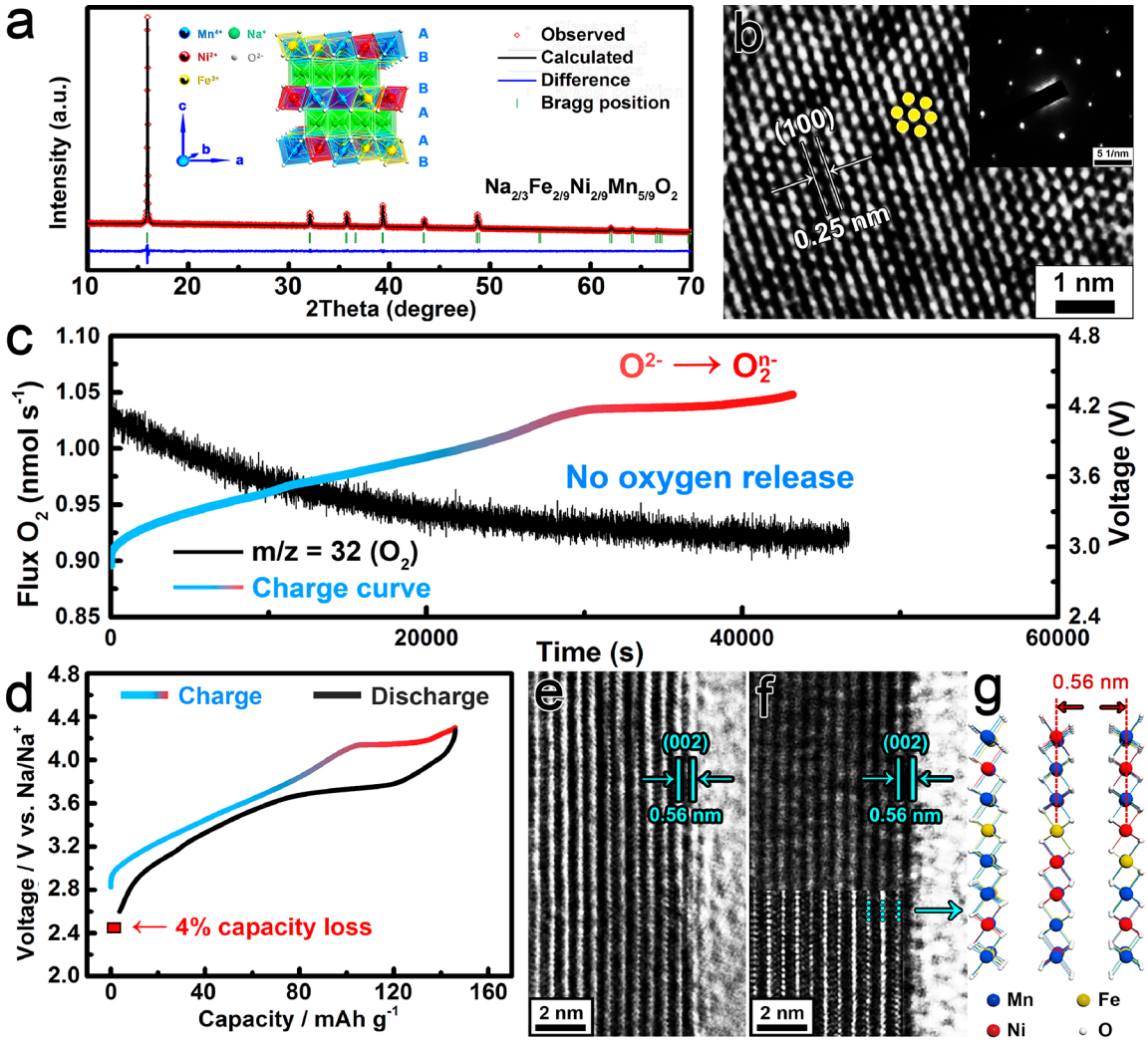

Figure 4. (a) XRD and Rietveld plots of the $Na_{2/3}Fe_{2/9}Ni_{2/9}Mn_{5/9}O_2$ sample. The inset shows the P2 type structure with "ABBAAB" arrangement. (b) HRTEM image of the $Na_{2/3}Fe_{2/9}Ni_{2/9}Mn_{5/9}O_2$ sample. The inset image is the corresponding SAED pattern. (c) In situ DEMS analysis of oxygen evolution during the first charge for $Na_{2/3}Fe_{2/9}Ni_{2/9}Mn_{5/9}O_2$ electrode. The current density is 10 μA mg^{-1}, and the cut off voltage is 4.3 V. (d) Galvanostatic charge/discharge curves of the $Na_{2/3}Fe_{2/9}Ni_{2/9}Mn_{5/9}O_2$ electrode and the irreversible capacity loss for the first cycle at 0.1 C. (e) HRTEM image at the pristine state. (f) HRTEM image after 1 cycle. (g) The P2 crystal structure for the surface layer.

100 plane with a distance of 0.25 nm. The corresponding SAED pattern in the inset of Figure 4b confirms the typical single-crystal feature of the $Na_{2/3}Fe_{2/9}Ni_{2/9}Mn_{5/9}O_2$ sample. XPS analysis for Ni, Mn, and O was carried out at different charge states in $Na_{2/3}Fe_{2/9}Ni_{2/9}Mn_{5/9}O_2$ (Figure S7). For the O element, the peak of 529.5 eV at the pristine stage refers to lattice O^{2-} anions. When charged to 4.15 V, the peak of O_2^{n-} species emerges at 530.5 eV, suggesting the triggering of oxygen activity.[33−37] With further charging to 4.3 V, the peak of O_2^{n-} is well maintained, indicating that the O^{2-}/O_2^{n-} couple participates in the charge compensation process at a high operating voltage. According to the in situ DEMS test (Figure 4c), no O_2 gas is detected during the whole charge process, proving that the oxygen release behavior at a high operating voltage has been successfully suppressed by Fe substitution. Meanwhile, the irreversible capacity loss has been reduced from 25% to 4% at the initial cycle (Figure 4d), demonstrating the improvement of the electrochemical reversibility after the suppressing of oxygen release.

HRTEM was used to observe the crystal structure evolution of $Na_{2/3}Fe_{2/9}Ni_{2/9}Mn_{5/9}O_2$ particles. At the pristine state (Figure 4e), the surface shows a P2 structure with a interlayer distance of 0.56 nm. After the charge/discharge process for one cycle, the surface structure shows no obvious change (Figure 4f); hence, the interlayer space is suitable for the Na^+ intercalation/deintercalation process. Even after 10 cycles, the P2 structure at the surface almost remains unchanged (Figure S5c). The corresponding XRD pattern of $Na_{2/3}Fe_{2/9}Ni_{2/9}Mn_{5/9}O_2$ is shown in Figure S5d. Compared with the surface lattice densification on $Na_{2/3}Ni_{1/3}Mn_{2/3}O_2$ particles, no surface reconstruction occurs on $Na_{2/3}Fe_{2/9}Ni_{2/9}Mn_{5/9}O_2$ after the charge/discharge process (Figure 4g). Therefore, Fe substitution plays a crucial role in suppressing oxygen release and surface densification during the electrochemical reaction.

Reductive Coupling Mechanism. XPS analysis at different states was used to understand the mechanism of Fe substitution on the suppressing of oxygen release at high operating voltage (Figure 5a). At the pristine stage, the peak at 711.8 eV of the Fe 2p core spectra is assigned to Fe^{3+}.[48,49] When charged to 4.15 V, the peak of Fe^{3+} shifts toward higher energy binding at 713.1 eV, indicative of the oxidation reaction of $Fe^{3+} \rightarrow Fe^{4+}$.[48] However, with further charging to 4.3 V, this peak unexpectedly moves

https://dx.doi.org/10.1021/acscentsci.9b01166
ACS Cent. Sci. 2020, 6, 232−240

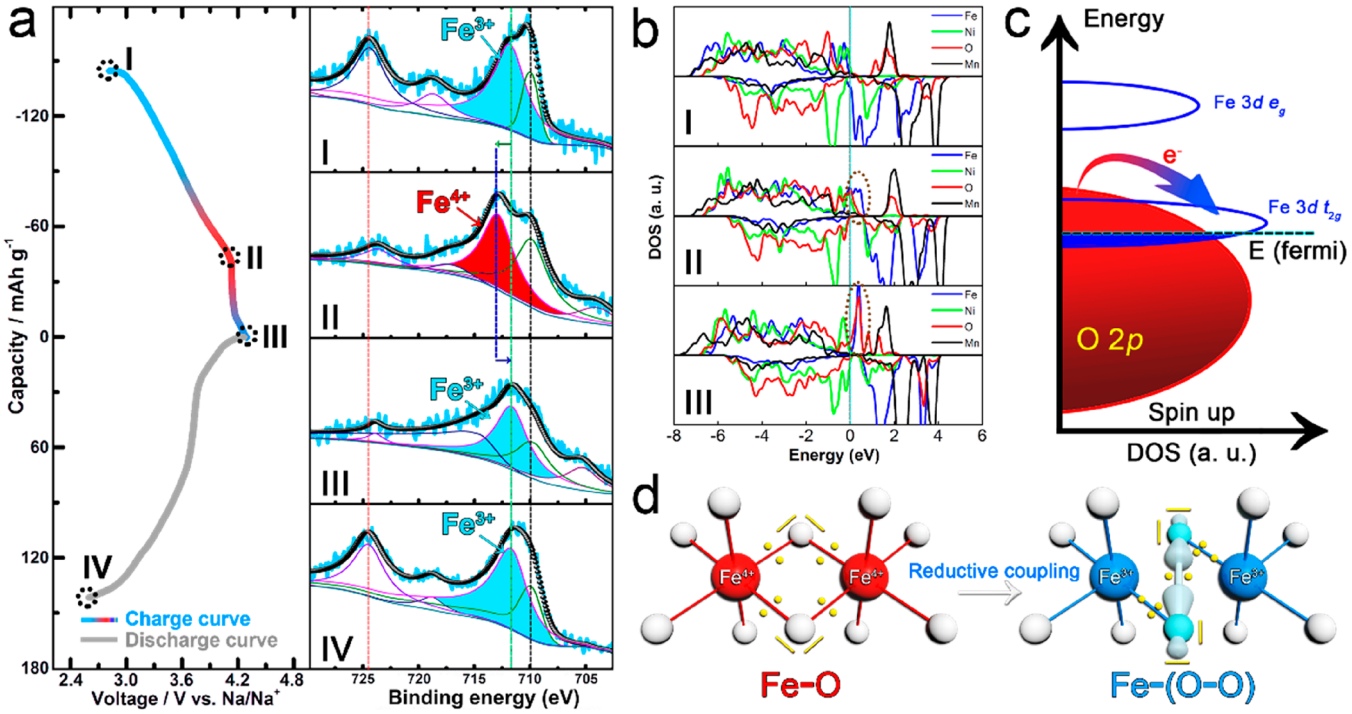

Figure 5. (a) XPS spectra of Fe 2p core at various charge states. (b) DOS of $Na_{2/3}Fe_{2/9}Ni_{2/9}Mn_{5/9}O_2$ at different charge states. (c) Schematic representation of the energy level versus DOS and the charge transfer from O 2p to Fe 3d. (d) Reductive coupling mechanism for the formation of Fe-(O−O) species. The oxidized Fe^{4+} at point II was reduced to Fe^{3+} at point III though electronic redistribution.

back to 711.8 eV, which means that the Fe^{4+} has been reduced to Fe^{3+} in this voltage region. A similar TM-reductive behavior was reported in the Li-rich $Li_2Ru_{1-y}Sn_yO_3$ cathode.[34] Ru^{5+} was reduced to Ru^{4+} at a high operating voltage, which is associated with a reductive coupling mechanism.

DOS was calculated at various states to elucidate the reductive coupling behavior in $Na_{2/3}Fe_{2/9}Ni_{2/9}Mn_{5/9}O_2$ (Figure 5b). At the initial stage (point I), the Ni and Fe 3d bands are near the Fermi level, and oxidation proceeds through removing electrons from the Ni and Fe 3d orbital. When charged to 4.15 V (point II), the O 2p band gets close to the Fermi level, and hence the lattice oxygen start to participate in the oxidation process. With further charging to 4.3 V (point III), O 2p states exceed the Fermi level, leading to the removal of electrons along with the creation of O-hole or O−O pairing.[38,43] Meanwhile, the Fe 3d bands are strongly hybridized with the O 2p band (dashed ellipse in Figure 5b, point II and point III), favoring the formation of a stable Fe-(O−O) bonding states through a charge-transfer system (O to Fe charge transfer, as shown in Figure 5c).[38,50−52] This reductive behavior of $Fe^{4+} \rightarrow Fe^{3+}$ is induced by the electronic redistribution from the Fe−O bonding state to a high covalent Fe-(O−O) bonding state (Figure 5d). The high covalent binding between the Fe and O−O peroxo-like species effectively prevents O_2 gas release, promoting the reversibility of O^{2-}/O_2^{n-} redox at a high operating voltage.

Structure Evolution and Electrochemical Performance. To analyze the structure evolution of $Na_{2/3}Ni_{1/3}Mn_{2/3}O_2$ during the charge/discharge process, ex situ XRD tests were carried out at various potentials (marked with *a*, *b*, *c*, *d*, *e*, *f*, *j*, *h*, and *i* in Figure 6a). From point *a* (initial state) to *d* (about the middle position of the 4.2 V plateau), the P2 phase is well maintained with only slight peak shifts. When the charge state reaches point *e* (4.3 V), a new peak (referred as 002′) appears at 21° with the weakening of the 002 peak, suggesting the phase transition of P2 → O2 in the voltage region from point *d* to *e*.[14,20] The two peaks marked with the "#" symbol belong to the hydrated phase.[15] After Fe substitution, the XRD patterns show no phase transition behavior during the whole charge/discharge process (Figure 6b).

Galvanostatic intermittent titration technique (GITT) was used to determine Na^+ diffusion coefficients of $Na_{2/3}Ni_{1/3}Mn_{2/3}O_2$ and $Na_{2/3}Fe_{2/9}Ni_{2/9}Mn_{5/9}O_2$ under different Na^+ concentrations (Figure 6c). When the Na^+ removal range is $0 \leq z \leq 1/3$, the Na^+ diffusion coefficient of $Na_{2/3}Ni_{1/3}Mn_{2/3}O_2$ is around 1 order of magnitude lower than that of $Na_{2/3}Fe_{2/9}Ni_{2/9}Mn_{5/9}O_2$ due to the existence of Na^+ vacancy ordering structure (Figure S8 and Figure S9). When the Na^+ removal range exceeded 1/3, the Na^+ diffusion coefficient of $Na_{2/3}Ni_{1/3}Mn_{2/3}O_2$ displays a dramatic fluctuation between 10^{-12} and 10^{-15} cm^2s^{-1}, while $Na_{2/3}Fe_{2/9}Ni_{2/9}Mn_{5/9}O_2$ shows a gradually decrease from 10^{-11} to 10^{-12} $cm^2\ s^{-1}$. Rate capability of $Na_{2/3}Ni_{1/3}Mn_{2/3}O_2$ and $Na_{2/3}Fe_{2/9}Ni_{2/9}Mn_{5/9}O_2$ are tested at different current densities (Figure 6d). $Na_{2/3}Ni_{1/3}Mn_{2/3}O_2$ electrode delivers a discharge capacity of 119 mAh g^{-1} at 0.1 C (1 C = 160 mAh g^{-1}), but only 17% (21 mAh g^{-1}) is retained at 5 C. In contrast, $Na_{2/3}Fe_{2/9}Ni_{2/9}Mn_{5/9}O_2$ shows a discharge capacity of 141 mAh g^{-1} at 0.1 C with a high retention of 45% (63 mAh g^{-1}) at 5 C due to its higher Na^+ mobility, which has been proven by GITT analysis. What is more, it should be noticed that the P2 phase in $Na_{2/3}Ni_{1/3}Mn_{2/3}O_2$ converts to the O2 phase (Figure 6a) at a high voltage region, while the P2 phase in $Na_{2/3}Fe_{2/9}Ni_{2/9}Mn_{5/9}O_2$ is well maintained (Figure 6b) during the whole charge/discharge process. The Na ion diffusion paths in the O2 and P2 structures are quite different. For the O2 structure, the migration of Na ions from one octahedron site to another requires two transits of the triangular face. For P2 structure, the diffusion of Na ions between two prismatic sites only needs to pass through one rectangular face. A

https://dx.doi.org/10.1021/acscentsci.9b01166
ACS Cent. Sci. 2020, 6, 232−240

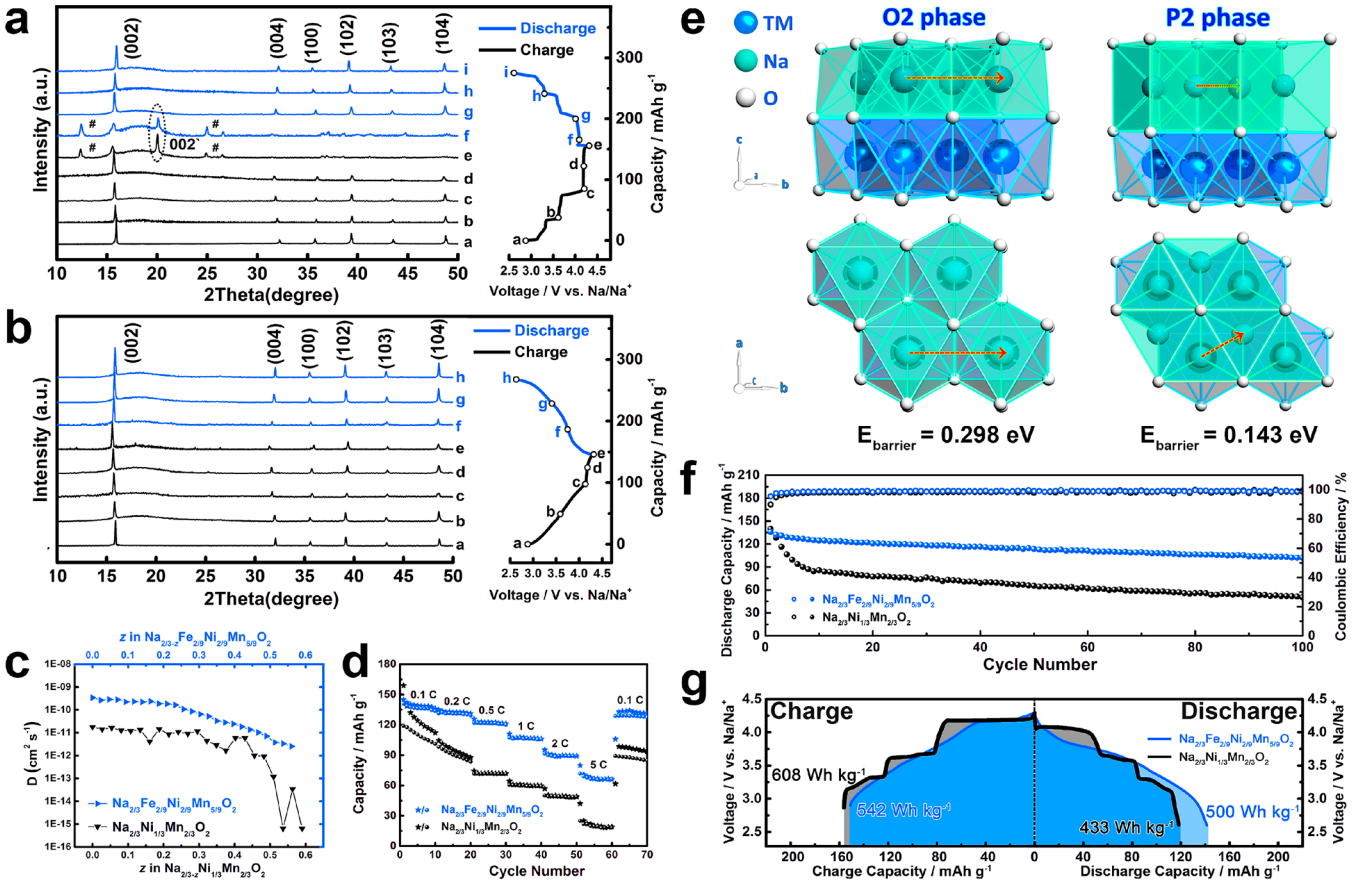

Figure 6. (a, b) Ex situ XRD patterns of $Na_{2/3}Ni_{1/3}Mn_{2/3}O_2$ and $Na_{2/3}Fe_{2/9}Ni_{2/9}Mn_{5/9}O_2$ at various potentials. (c) The Na^+ diffusion coefficients in $Na_{2/3}Ni_{1/3}Mn_{2/3}O_2$ and $Na_{2/3}Fe_{2/9}Ni_{2/9}Mn_{5/9}O_2$ calculated from GITT. (d) Rate capability of $Na_{2/3}Ni_{1/3}Mn_{2/3}O_2$ and $Na_{2/3}Fe_{2/9}Ni_{2/9}Mn_{5/9}O_2$. (e) The diffusion paths of Na^+ in O2 and P2 phase and the corresponding energy barrier. (f) Cycling stability of $Na_{2/3}Ni_{1/3}Mn_{2/3}O_2$ and $Na_{2/3}Fe_{2/9}Ni_{2/9}Mn_{5/9}O_2$ at 0.5 C. (g) Comparison of energy density for $Na_{2/3}Ni_{1/3}Mn_{2/3}O_2$ and $Na_{2/3}Fe_{2/9}Ni_{2/9}Mn_{5/9}O_2$.

nudged elastic band (NEB) calculation was carried out to further study the energy barrier in the O2 and P2 structure (Figure 6e). The energy barrier in O2 phase is 0.298 eV, while that in the P2 phase is 0.143 eV, indicating the higher Na^+ mobility in $Na_{2/3}Fe_{2/9}Ni_{2/9}Mn_{5/9}O_2$ with the stable P2 phase.

Cycling performance and the corresponding Coulombic efficiency (CE) were evaluated at 0.5 C current density (Figure 6f). Compared with the low CE of 88.5% in the $Na_{2/3}Ni_{1/3}Mn_{2/3}O_2$ electrode, the $Na_{2/3}Fe_{2/9}Ni_{2/9}Mn_{5/9}O_2$ electrode shows 95.4% CE at the initial cycle. After 100 cycles, the discharge capacity of $Na_{2/3}Ni_{1/3}Mn_{2/3}O_2$ shows a rapid decay, and only 44% capacity (58.4 mAh g^{-1}) is retained, while 78% (102.1 mAh g^{-1}) discharge capacity is maintained for $Na_{2/3}Fe_{2/9}Ni_{2/9}Mn_{5/9}O_2$ electrode. The energy densities of $Na_{2/3}Ni_{1/3}Mn_{2/3}O_2$ and $Na_{2/3}Fe_{2/9}Ni_{2/9}Mn_{5/9}O_2$ are shown in Figure 6g. Although $Na_{2/3}Ni_{1/3}Mn_{2/3}O_2$ shows a large energy density of 608 Wh kg^{-1} during the charge process, only 71% (433 Wh kg^{-1}) is obtained during the subsequent discharge process. In contrast, $Na_{2/3}Fe_{2/9}Ni_{2/9}Mn_{5/9}O_2$ delivers 542 Wh kg^{-1} during the charge process and a high retention of 92% (500 Wh kg^{-1}) is achieved during the subsequent discharge process. The superior reversibility of O^{2-}/O_2^{n-} redox, rate capability, cycling stability, and energy density retention of $Na_{2/3}Fe_{2/9}Ni_{2/9}Mn_{5/9}O_2$ are attributed to Fe substitution, which effectively suppresses the oxygen release, surface lattice densification, and phase transition during the electrochemical reaction.

CONCLUSION

In summary, we prove the existence of $O^{2-}/O_2^{n-}/O_2$ evolution and solved the oxygen release problem in $Na_{2/3}Ni_{1/3}Mn_{2/3}O_2$. At the 4.2 V plateau, the oxygen functions as the electron donor, and the irreversible $O^{2-}/O_2^{n-}/O_2$ evolution occurs due to the lack of TM-O hybridization. The loss of oxygen causes the surface densification of $Na_{2/3}Ni_{1/3}Mn_{2/3}O_2$ particles, and this dense structure is not suitable for Na^+ intercalation. Therefore, the formation of an inactive dense layer at the initial cycle is considered as the main reason for the irreversible capacity loss. The oxygen release behavior in $Na_{2/3}Ni_{1/3}Mn_{2/3}O_2$ can be greatly suppressed by Fe substitution due to the formation of the Fe-(O−O) species associated with the reductive coupling behavior, which preserves the reversibility of O^{2-}/O_2^{n-} redox reaction at a high operating voltage. As a result, the irreversible capacity loss at the initial cycle is reduced from 25% to 4%, and the capacity retention increases from 42% to 78% after 100 cycles. The understanding of oxygen release behavior in the Na-deficient cathode and the strategy for suppressing of oxygen release offer a new perspective for developing high-performance cathode materials with high reversibility and long cycling stability for SIBs.

EXPERIMENTAL PROCEDURES

The details of experimental procedures are provided in Supporting Information.

https://dx.doi.org/10.1021/acscentsci.9b01166
ACS Cent. Sci. 2020, 6, 232−240

■ ASSOCIATED CONTENT

Supporting Information

The Supporting Information is available free of charge at https://pubs.acs.org/doi/10.1021/acscentsci.9b01166.

Experimental section; characterization method; additional figures and tables (PDF)

■ AUTHOR INFORMATION

Corresponding Authors

Renyuan Zhang − *Institute of New Energy for Vehicles, Shanghai Key Laboratory for Development and Application of Metallic Functional Materials, School of Materials Science and Engineering, Tongji University, Shanghai 201804, P. R. China;* orcid.org/0000-0001-5979-5512; Email: ryzhang@tongji.edu.cn

Yunhui Huang − *Institute of New Energy for Vehicles, Shanghai Key Laboratory for Development and Application of Metallic Functional Materials, School of Materials Science and Engineering, Tongji University, Shanghai 201804, P. R. China;* Email: huangyh@tongji.edu.cn

Authors

Yi Zhang − *Institute of New Energy for Vehicles, Shanghai Key Laboratory for Development and Application of Metallic Functional Materials, School of Materials Science and Engineering, Tongji University, Shanghai 201804, P. R. China*

Miaomiao Wu − *Institute of New Energy for Vehicles, Shanghai Key Laboratory for Development and Application of Metallic Functional Materials, School of Materials Science and Engineering, Tongji University, Shanghai 201804, P. R. China*

Jiwei Ma − *Institute of New Energy for Vehicles, Shanghai Key Laboratory for Development and Application of Metallic Functional Materials, School of Materials Science and Engineering, Tongji University, Shanghai 201804, P. R. China;* orcid.org/0000-0003-4209-7667

Guangfeng Wei − *Shanghai Key Laboratory of Chemical Assessment and Sustainability, School of Chemical Science and Engineering, Tongji University, Shanghai 200092, P. R. China*

Yun Ling − *Department of Chemistry, Fudan University, Shanghai 200433, P. R. China;* orcid.org/0000-0002-6956-4504

Complete contact information is available at: https://pubs.acs.org/10.1021/acscentsci.9b01166

Notes

The authors declare no competing financial interest.

■ ACKNOWLEDGMENTS

We gratefully acknowledge the financial support from the National Natural Science Foundation of China (Grant Nos. 51602221 and 51632001), Shanghai Municipal Natural Science Foundation (16ZR1438400), National Key R&D Program of China under Grant No. 2018YFB0905400, and the Fundamental Research Funds for the Central Universities.

■ REFERENCES

(1) Vaalma, C.; Buchholz, D.; Weil, M.; Passerini, S. A cost and resource analysis of sodium-ion batteries. *Nat. Rev. Mater.* **2018**, *3*, 18013.

(2) Palomares, V.; Serras, P.; Villaluenga, I.; Hueso, K. B.; Carretero-Gonzalez, J.; Rojo, T. Na-ion batteries, recent advances and present challenges to become low cost energy storage systems. *Energy Environ. Sci.* **2012**, *5*, 5884−5901.

(3) Fang, Y.; Yu, X.-Y.; Lou, X. W. D. Nanostructured electrode materials for advanced sodium-ion batteries. *Matter* **2019**, *1*, 90−114.

(4) Liu, T. F.; Zhang, Y. P.; Jiang, Z. G.; Zeng, X. Q.; Ji, J. P.; Li, Z. H.; Gao, X. H.; Sun, M. H.; Lin, Z.; Ling, M.; Zheng, J. C.; Liang, C. D. Exploring competitive features of stationary sodium ion batteries for electrochemical energy storage. *Energy Environ. Sci.* **2019**, *12*, 1512−1533.

(5) Han, M. H.; Gonzalo, E.; Singh, G.; Rojo, T. A comprehensive review of sodium layered oxides: powerful cathodes for Na-ion batteries. *Energy Environ. Sci.* **2015**, *8*, 81−102.

(6) Nayak, P. K.; Yang, L.; Brehm, W.; Adelhelm, P. From Lithium-Ion to Sodium-Ion Batteries: Advantages, Challenges, and Surprises. *Angew. Chem., Int. Ed.* **2018**, *57*, 102−120.

(7) Zhou, W.; Li, Y.; Xin, S.; Goodenough, J. B. Rechargeable Sodium All-Solid-State Battery. *ACS Cent. Sci.* **2017**, *3*, 52−57.

(8) Delmas, C.; Braconnier, J.-J.; Fouassier, C.; Hagenmuller, P. Electrochemical intercalation of sodium in Na_xCoO_2 bronzes. *Solid State Ionics* **1981**, *3*, 165−169.

(9) Velikokhatnyi, O. I.; Chang, C.-C.; Kumta, P. N. Phase stability and electronic structure of $NaMnO_2$. *J. Electrochem. Soc.* **2003**, *150*, A1262−A1266.

(10) Berthelot, R.; Carlier, D.; Delmas, C. Electrochemical investigation of the P2−Na_xCoO_2 phase diagram. *Nat. Mater.* **2011**, *10*, 74−80.

(11) Guignard, M.; Didier, C.; Darriet, J.; Bordet, P.; Elkaïm, E.; Delmas, C. P2-Na_xVO_2 system as electrodes for batteries and electron-correlated materials. *Nat. Mater.* **2013**, *12*, 74−80.

(12) Zhang, Y.; Zhang, R.; Huang, Y. Air-stable Na_xTMO_2 cathodes for sodium storage. *Front. Chem.* **2019**, *7*, 335.

(13) Li, Y. J.; Gao, Y. R.; Wang, X. F.; Shen, X.; Kong, Q. Y.; Yu, R. C.; Lu, G.; Wang, Z. X.; Chen, L. Q. Iron migration and oxygen oxidation during sodium extraction from $NaFeO_2$. *Nano Energy* **2018**, *47*, 519−526.

(14) Lu, Z.; Dahn, J. R. In situ X-Ray Diffraction study of P2 $Na_{2/3}[Ni_{1/3}Mn_{2/3}]O_2$. *J. Electrochem. Soc.* **2001**, *148*, A1225−A1229.

(15) Lu, Z.; Dahn, J. R. Intercalation of water in P2, T2 and O2 structure $A_z[Co_xNi_{1/3-x}Mn_{2/3}]O_2$. *Chem. Mater.* **2001**, *13*, 1252−1257.

(16) Zheng, L.; Li, J.; Obrovac, M. N. Crystal structures and electrochemical performance of air-stable $Na_{2/3}Ni_{1/3-x}Cu_xMn_{2/3}O_2$ in sodium cells. *Chem. Mater.* **2017**, *29*, 1623−1631.

(17) Yang, Q.; Wang, P. F.; Guo, J. Z.; Chen, Z. M.; Pang, W. L.; Huang, K. C.; Guo, Y. G.; Wu, X. L.; Zhang, J. P. Advanced P2-$Na_{2/3}Ni_{1/3}Mn_{7/12}Fe_{1/12}O_2$ cathode material with suppressed P2−O2 phase transition toward high-performance sodium-Ion battery. *ACS Appl. Mater. Interfaces* **2018**, *10*, 34272−34282.

(18) Wang, L.; Sun, Y.-G.; Hu, L.-L.; Piao, J.-Y.; Guo, J.; Manthiram, A.; Ma, J.; Cao, A.-M. Copper-substituted $Na_{0.67}Ni_{0.3-x}Cu_xMn_{0.7}O_2$ cathode materials for sodium-ion batteries with suppressed P2-O2 phase transition. *J. Mater. Chem. A* **2017**, *5*, 8752−8761.

(19) Tapia Ruiz, N.; Dose, W. M.; Sharma, N.; Chen, H.; Heath, J.; Somerville, J. W.; Maitra, U.; Islam, M. S.; Bruce, P. G. High voltage structural evolution and enhanced Na-ion diffusion in P2-$Na_{2/3}Ni_{1/3-x}Mg_xMn_{2/3}O_2$ ($0 \le x \le 0.2$) cathodes from diffraction, electrochemical and ab initio studies. *Energy Environ. Sci.* **2018**, *11*, 1470−1479.

(20) Wang, P. F.; You, Y.; Yin, Y. X.; Wang, Y. S.; Wan, L. J.; Gu, L.; Guo, Y. G. Suppressing the P2-O2 phase transition of $Na_{0.67}Mn_{0.67}Ni_{0.33}O_2$ by magnesium substitution for improved sodium-ion batteries. *Angew. Chem., Int. Ed.* **2016**, *55*, 7445−7449.

(21) Singh, G.; Tapia-Ruiz, N.; Lopez del Amo, J. M.; Maitra, U.; Somerville, J. W.; Armstrong, A. R.; Martinez de Ilarduya, J.; Rojo, T.; Bruce, P. G. High voltage Mg-doped $Na_{0.67}Ni_{0.3-x}Mg_xMn_{0.7}O_2$ (x = 0.05, 0.1) Na-Ion cathodes with enhanced stability and rate capability. *Chem. Mater.* **2016**, *28*, 5087−5094.

(22) Ma, C.; Alvarado, J.; Xu, J.; Clement, R. J.; Kodur, M.; Tong, W.; Grey, C. P.; Meng, Y. S. Exploring oxygen activity in the high energy P2-Type $Na_{0.78}Ni_{0.23}Mn_{0.69}O_2$ cathode material for Na-Ion batteries. *J. Am. Chem. Soc.* **2017**, *139*, 4835−4845.

(23) Risthaus, T.; Zhou, D.; Cao, X.; He, X.; Qiu, B.; Wang, J.; Zhang, L.; Liu, Z.; Paillard, E.; Schumacher, G.; Winter, M.; Li, J. A high-capacity P2 $Na_{2/3}Ni_{1/3}Mn_{2/3}O_2$ cathode material for sodium ion batteries with oxygen activity. *J. Power Sources* **2018**, *395*, 16−24.
(24) Wang, K.; Yan, P.; Sui, M. Phase transition induced cracking plaguing layered cathode for sodium-ion battery. *Nano Energy* **2018**, *54*, 148−155.
(25) Wu, X.; Guo, J.; Wang, D.; Zhong, G.; McDonald, M. J.; Yang, Y. P2-type $Na_{0.66}Ni_{0.33-x}Zn_xMn^{0.67}O_2$ as new high-voltage cathode materials for sodium-ion batteries. *J. Power Sources* **2015**, *281*, 18−26.
(26) Liu, Y.; Fang, X.; Zhang, A.; Shen, C.; Liu, Q.; Enaya, H. A.; Zhou, C. Layered P2-$Na_{2/3}[Ni_{1/3}Mn_{2/3}]O_2$ as high-voltage cathode for sodium-ion batteries: The capacity decay mechanism and Al_2O_3 surface modification. *Nano Energy* **2016**, *27*, 27−34.
(27) Ramasamy, H. V.; Kaliyappan, K.; Thangavel, R.; Aravindan, V.; Kang, K.; Kim, D. U.; Park, Y.; Sun, X.; Lee, Y.-S. Cu-doped P2-$Na_{0.5}Ni_{0.33}Mn_{0.67}O_2$ encapsulated with MgO as a novel high voltage cathode with enhanced Na-storage properties. *J. Mater. Chem. A* **2017**, *5*, 8408−8415.
(28) Fu, Z.; Hu, J.; Hu, W.; Yang, S.; Luo, Y. Quantitative analysis of Ni^{2+}/Ni^{3+} in $Li[Ni_xMn_yCo_z]O_2$ cathode materials: Non-linear least-squares fitting of XPS spectra. *Appl. Surf. Sci.* **2018**, *441*, 1048−1056.
(29) Inamdar, A. I.; Sonavane, A. C.; Pawar, S. M.; Kim, Y.; Kim, J. H.; Patil, P. S.; Jung, W.; Im, H.; Kim, D.-Y.; Kim, H. Electrochromic and electrochemical properties of amorphous porous nickel hydroxide thin films. *Appl. Surf. Sci.* **2011**, *257*, 9606−9611.
(30) Hemalatha, K.; Jayakumar, M.; Bera, P.; Prakash, A. S. Improved electrochemical performance of $Na_{0.67}MnO_2$ through Ni and Mg substitution. *J. Mater. Chem. A* **2015**, *3*, 20908−20912.
(31) Wang, H.-Y.; Hsu, Y.-Y.; Chen, R.; Chan, T.-S.; Chen, H. M.; Liu, B. Ni^{3+} induced formation of active NiOOH on the spinel Ni−Co oxide surface for efficient oxygen evolution reaction. *Adv. Energy Mater.* **2015**, *5*, 1500091.
(32) Guo, S. H.; Yu, H. J.; Liu, P.; Ren, Y.; Zhang, T.; Chen, M. W.; Ishida, M.; Zhou, H. S. High-performance symmetric sodium-ion batteries using a new, bipolar O3-type material, $Na_{0.8}Ni_{0.4}Ti_{0.6}O_2$. *Energy Environ. Sci.* **2015**, *8*, 1237−1244.
(33) Saubanere, M.; McCalla, E.; Tarascon, J. M.; Doublet, M. L. The intriguing question of anionic redox in high-energy density cathodes for Li-ion batteries. *Energy Environ. Sci.* **2016**, *9*, 984−991.
(34) Sathiya, M.; Rousse, G.; Ramesha, K.; Laisa, C. P.; Vezin, H.; Sougrati, M. T.; Doublet, M. L.; Foix, D.; Gonbeau, D.; Walker, W.; Prakash, A. S.; Ben Hassine, M.; Dupont, L.; Tarascon, J. M. Reversible anionic redox chemistry in high-capacity layered-oxide electrodes. *Nat. Mater.* **2013**, *12*, 827−835.
(35) Grimaud, A.; Hong, W. T.; Shao-Horn, Y.; Tarascon, J. M. Anionic redox processes for electrochemical devices. *Nat. Mater.* **2016**, *15*, 121−126.
(36) Sathiya, M.; Abakumov, A. M.; Foix, D.; Rousse, G.; Ramesha, K.; Saubanere, M.; Doublet, M. L.; Vezin, H.; Laisa, C. P.; Prakash, A. S.; Gonbeau, D.; VanTendeloo, G.; Tarascon, J. M. Origin of voltage decay in high-capacity layered oxide electrodes. *Nat. Mater.* **2015**, *14*, 230−238.
(37) Pearce, P. E.; Perez, A. J.; Rousse, G.; Saubanère, M.; Batuk, D.; Foix, D.; McCalla, E.; Abakumov, A. M.; Van Tendeloo, G.; Doublet, M.-L.; Tarascon, J.-M. Evidence for anionic redox activity in a tridimensional-ordered Li-rich positive electrode β-Li_2IrO_3. *Nat. Mater.* **2017**, *16*, 580.
(38) Ben Yahia, M.; Vergnet, J.; Saubanere, M.; Doublet, M. L. Unified picture of anionic redox in Li/Na-ion batteries. *Nat. Mater.* **2019**, *18*, 496−502.
(39) Assat, G.; Tarascon, J. M. Fundamental understanding and practical challenges of anionic redox activity in Li-ion batteries. *Nat. Energy* **2018**, *3*, 373−386.
(40) Perez, A. J.; Jacquet, Q.; Batuk, D.; Iadecola, A.; Saubanère, M.; Rousse, G.; Larcher, D.; Vezin, H.; Doublet, M.-L.; Tarascon, J.-M. Approaching the limits of cationic and anionic electrochemical activity with the Li-rich layered rocksalt Li_3IrO_4. *Nat. Energy* **2017**, *2*, 954−962.
(41) Savin, A.; Nesper, R.; Wengert, S.; Fässler, T. F. ELF: The Electron Localization Function. *Angew. Chem., Int. Ed. Engl.* **1997**, *36*, 1808−1832.
(42) Lai, W.; Wang, Y.; Morelli, D. T.; Lu, X. From bonding asymmetry to anharmonic rattling in $Cu_{12}Sb_4S_{13}$ Tetrahedrites: when Lone-Pair electrons are not so lonely. *Adv. Funct. Mater.* **2015**, *25*, 3648−3657.
(43) Xiao, R.; Li, H.; Chen, L. Density Functional Investigation on Li_2MnO_3. *Chem. Mater.* **2012**, *24*, 4242−4251.
(44) Luo, K.; Roberts, M. R.; Hao, R.; Guerrini, N.; Pickup, D. M.; Liu, Y.-S.; Edström, K.; Guo, J.; Chadwick, A. V.; Duda, L. C.; Bruce, P. G. Charge-compensation in 3d-transition-metal-oxide intercalation cathodes through the generation of localized electron holes on oxygen. *Nat. Chem.* **2016**, *8*, 684.
(45) Mu, L.; Lin, R.; Xu, R.; Han, L.; Xia, S.; Sokaras, D.; Steiner, J. D.; Weng, T.-C.; Nordlund, D.; Doeff, M. M.; Liu, Y.; Zhao, K.; Xin, H. L.; Lin, F. Oxygen release Induced chemomechanical breakdown of layered cathode materials. *Nano Lett.* **2018**, *18*, 3241−3249.
(46) Li, Q.; Yao, Z.; Lee, E.; Xu, Y.; Thackeray, M. M.; Wolverton, C.; Dravid, V. P.; Wu, J. Dynamic imaging of crystalline defects in lithium-manganese oxide electrodes during electrochemical activation to high voltage. *Nat. Commun.* **2019**, *10*, 1692.
(47) Yan, P.; Zheng, J.; Chen, T.; Luo, L.; Jiang, Y.; Wang, K.; Sui, M.; Zhang, J.; Zhang, S.; Wang, C. Coupling of electrochemically triggered thermal and mechanical effects to aggravate failure in a layered cathode. *Nat. Commun.* **2018**, *9*, 2437.
(48) Rajagopalan, R.; Chen, B.; Zhang, Z.; Wu, X. L.; Du, Y.; Huang, Y.; Li, B.; Zong, Y.; Wang, J.; Nam, G. H.; Sindoro, M.; Dou, S. X.; Liu, H. K.; Zhang, H. Improved reversibility of $Fe^{(3+)}/Fe^{(4+)}$ redox couple in sodium super ion conductor type $Na_3Fe_2(PO_4)_3$ for sodium-ion batteries. *Adv. Mater.* **2017**, *29*, 1605694.
(49) Biesinger, M. C.; Payne, B. P.; Grosvenor, A. P.; Lau, L. W. M.; Gerson, A. R.; Smart, R. S. C. Resolving surface chemical states in XPS analysis of first row transition metals, oxides and hydroxides: Cr, Mn, Fe, Co and Ni. *Appl. Surf. Sci.* **2011**, *257*, 2717−2730.
(50) Zaanen, J.; Sawatzky, G. A.; Allen, J. W. Band gaps and electronic structure of transition-metal compounds. *Phys. Rev. Lett.* **1985**, *55*, 418−421.
(51) Yabuuchi, N.; Nakayama, M.; Takeuchi, M.; Komaba, S.; Hashimoto, Y.; Mukai, T.; Shiiba, H.; Sato, K.; Kobayashi, Y.; Nakao, A.; Yonemura, M.; Yamanaka, K.; Mitsuhara, K.; Ohta, T. Origin of stabilization and destabilization in solid-state redox reaction of oxide ions for lithium-ion batteries. *Nat. Commun.* **2016**, *7*, 13814.
(52) Mortemard de Boisse, B.; Liu, G.; Ma, J.; Nishimura, S.-i.; Chung, S.-C.; Kiuchi, H.; Harada, Y.; Kikkawa, J.; Kobayashi, Y.; Okubo, M.; Yamada, A. Intermediate honeycomb ordering to trigger oxygen redox chemistry in layered battery electrode. *Nat. Commun.* **2016**, *7*, 11397−11397.

https://dx.doi.org/10.1021/acscentsci.9b01166
ACS Cent. Sci. 2020, 6, 232−240